AGU PUBLICATIONS

JGR

Journal of Geophysical Research: Atmospheres

RESEARCH ARTICLE
10.1002/2014JD022483

Key Points:
- Detectability of regional changes in CO_2 fluxes by space-based lidar
- Permafrost thawing flux perturbation readily detectable by ASCENDS-like mission
- Southern Ocean ENSO-related flux variability detectable as zonal change

Supporting Information:
- Figures S1–S8

Correspondence to:
D. M. Hammerling,
dorith@ucar.edu

Citation:
Hammerling, D. M., S. R. Kawa, K. Schaefer, S. Doney, and A. M. Michalak (2015), Detectability of CO_2 flux signals by a space-based lidar mission, *J. Geophys. Res. Atmos.*, *120*, 1794–1807, doi:10.1002/2014JD022483.

Received 25 AUG 2014
Accepted 5 JAN 2015
Accepted article online 8 JAN 2015
Published online 11 MAR 2015

Detectability of CO_2 flux signals by a space-based lidar mission

Dorit M. Hammerling[1,2], S. Randolph Kawa[3], Kevin Schaefer[4], Scott Doney[5], and Anna M. Michalak[6]

[1]Department of Civil and Environmental Engineering, University of Michigan, Ann Arbor, Michigan, USA, [2]Now at Institute for Mathematics Applied to Geosciences, National Center for Atmospheric Research, Boulder, Colorado, USA, [3]NASA Goddard Space Flight Center, Greenbelt, Maryland, USA, [4]National Snow and Ice Data Center, Cooperative Institute for Research in Environmental Sciences, University of Colorado at Boulder, Boulder, Colorado, USA, [5]Department of Marine Chemistry and Geochemistry, Woods Hole Oceanographic Institution, Woods Hole, Massachusetts, USA, [6]Department of Global Ecology, Carnegie Institution for Science, Stanford, California, USA

Abstract Satellite observations of carbon dioxide (CO_2) offer novel and distinctive opportunities for improving our quantitative understanding of the carbon cycle. Prospective observations include those from space-based lidar such as the active sensing of CO_2 emissions over nights, days, and seasons (ASCENDS) mission. Here we explore the ability of such a mission to detect regional changes in CO_2 fluxes. We investigate these using three prototypical case studies, namely, the thawing of permafrost in the northern high latitudes, the shifting of fossil fuel emissions from Europe to China, and changes in the source/sink characteristics of the Southern Ocean. These three scenarios were used to design signal detection studies to investigate the ability to detect the unfolding of these scenarios compared to a baseline scenario. Results indicate that the ASCENDS mission could detect the types of signals investigated in this study, with the caveat that the study is based on some simplifying assumptions. The permafrost thawing flux perturbation is readily detectable at a high level of significance. The fossil fuel emission detectability is directly related to the strength of the signal and the level of measurement noise. For a nominal (lower) fossil fuel emission signal, only the idealized noise-free instrument test case produces a clearly detectable signal, while experiments with more realistic noise levels capture the signal only in the higher (exaggerated) signal case. For the Southern Ocean scenario, differences due to the natural variability in the El Niño–Southern Oscillation climatic mode are primarily detectable as a zonal increase.

1. Introduction

Satellite observations of carbon dioxide (CO_2) offer novel and distinctive opportunities for improving our quantitative understanding of the carbon cycle, which is an important scientific and societal challenge with anthropogenic CO_2 emissions still on the rise. Prospective new observations include those from space-based lidar such as the active sensing of CO_2 emissions over nights, days, and seasons (ASCENDS) mission, which is proposed in "Earth Science and Applications from Space: National Imperatives for the Next Decade" [*National Research Council*, 2007] (henceforth referred to as the decadal survey). Notable features of this mission include its ability to sample at night and at high latitudes. These conditions are prohibitive to passive missions, such as the Greenhouse gases Observing SATellite [e.g., *Kuze et al.*, 2009; *Yokota et al.*, 2009] and the Orbiting Carbon Observatory-2 missions [e.g., *Crisp et al.*, 2004], due to their reliance on reflected sunlight. The lidar measurement technique proposed for the ASCENDS mission further enables observing through some clouds and aerosols [*Ehret et al.*, 2008], which also represent impediments and potential sources of bias for passive missions [e.g., *Mao and Kawa*, 2004]. Extensive instrument design research and development are ongoing, and proof of concept and validation studies indicate that ASCENDS will be able to provide high-precision, unbiased observations with improved spatial coverage compared to passive missions [e.g., *Spiers et al.*, 2011; *Abshire et al.*, 2010; *Kawa et al.*, 2010].

The primary goals of the ASCENDS mission are to address open questions in carbon cycle science that focus on the identification of changing source/sink characteristics that are difficult to observe using other current or anticipated observations. These goals were first articulated in the decadal survey [*National Research Council*, 2007] and later refined in an ASCENDS mission NASA Science Definition and Planning Workshop [*Active sensing of CO_2 emissions over nights, days, and seasons (ASCENDS) Workshop Steering Committee*, 2008].

They include detecting changes in the northern high-latitude sources and sinks, detecting changes in Southern Ocean source/sink characteristics, constraining anthropogenic CO_2 emissions, and increasing our understanding of biospheric carbon dynamics by differentiating photosynthetic and respiration fluxes [*ASCENDS Workshop Steering Committee*, 2008]. CO_2 fluxes in the northern high latitudes and in the Southern Ocean may change substantially as climate evolves, for example, and it is crucial to detect and attribute such changes quickly as they could lead to large increases in atmospheric CO_2 concentrations and subsequent shifts in climate dynamics [e.g., *Canadell et al*., 2010].

Guided by these stated goals, this study explores the extent to which a space-based lidar mission, using the ASCENDS mission concept as a guideline, can indeed contribute to these pertinent carbon cycle science questions. We specifically focus on the ability of such a mission to detect regional changes in fossil fuel emissions, high-latitude CO_2 fluxes, and CO_2 fluxes in the Southern Ocean. We investigate these using three prototypical case studies, namely, the thawing of permafrost in the northern high latitudes, the shifting of fossil fuel emissions from Europe to China, and changes in the source/sink characteristics of the Southern Ocean related to the El Niño–Southern Oscillation (ENSO). Realistic flux scenarios are defined for each of these prototypical case studies within the anticipated time frame of the ASCENDS mission (i.e., the early to mid-2020s). These flux scenarios, combined with a common set of baseline fluxes, form the basis of the presented analysis.

One can view the experimental setup as a hypothesis testing setup to answer the question if and how the CO_2 concentration fields resulting from the baseline and perturbation fluxes, as observed by an ASCENDS-like mission, are distinguishable. To that end, the three scenarios described above are used in Observing System Simulations Experiments (OSSEs) to investigate whether an ASCENDS-like mission will have the ability to identify the changes in atmospheric CO_2 distributions associated with the changes in fluxes represented in each scenario. We apply the geostatistical mapping approach developed in *Hammerling et al*. [2012a, 2012b] to generate global CO_2 maps based on the ASCENDS-like sampling of the atmospheric CO_2 distribution resulting from each flux scenario and characterize the time required to observe statistically significant changes in the inferred global CO_2 distribution, given varying assumptions about measurement uncertainty.

2. Model-Simulated Data

The study is based on simulated data described below. The study period represents a full year of the expected ASCENDS mission data.

2.1. Baseline CO_2 Atmosphere

We use the parameterized chemistry and transport model (PCTM) to produce a simulated distribution of atmospheric CO_2 variability in space and time [*Kawa et al*., 2004] based on the baseline and perturbation scenarios. Model transport is driven by real-time analyzed meteorology from the Goddard Earth Observing System version 5 Modern Era Retrospective-Analysis for Research and Applications (MERRA) [*Rienecker et al*., 2011] for 2007. CO_2 surface fluxes for the baseline run include terrestrial vegetation physiological processes and biomass burning from Carnegie-Ames-Stanford approach (CASA)-Global Fire Emissions Database version 3 [*Randerson et al*., 1996; *van der Werf et al*., 2010], seasonally varying climatological ocean fluxes from *Takahashi et al*. [2002], and fossil fuel burning from the Carbon Dioxide Information Analysis Center (CDIAC) database [*Andres et al*., 2009]. CASA fluxes are driven by MERRA data, which result in meteorologically driven correspondence in the synoptic variability in the surface fluxes and atmospheric transport. The monthly CASA fluxes are downscaled to 3 hourly fluxes in the method of *Olsen and Randerson* [2004] as described by, e.g., *Chatterjee et al.* [2012] and *Shiga et al.* [2013]. The annual integral for the CASA fluxes is 1.53 Pg/yr, representing a net source largely due to high respiration in 2007. The average yearly CASA flux for the period of 1997 to 2012 is 0.133 Pg/yr. The CASA fluxes used in this study are available at the North American Carbon Data archive (http://nacp-files.nacarbon.org/nacp-kawa-01/). PCTM CO_2 output has been extensively compared to in situ and remote sensing observations at a wide variety of sites, and in most cases, the model simulates diurnal to synoptic to seasonal variability with a high degree of fidelity [e.g., *Law et al*., 2008a; *Parazoo et al*., 2008; *Bian et al*., 2006; *Kawa et al*., 2004]. For the simulations here, the model is run on a 1°×1.25° latitude/longitude grid with 56 vertical levels and hourly output. We use 2007 meteorological, cloud and aerosol, and reflectivity data for all components employed in the derivation of the simulated ASCENDS CO_2 observations.

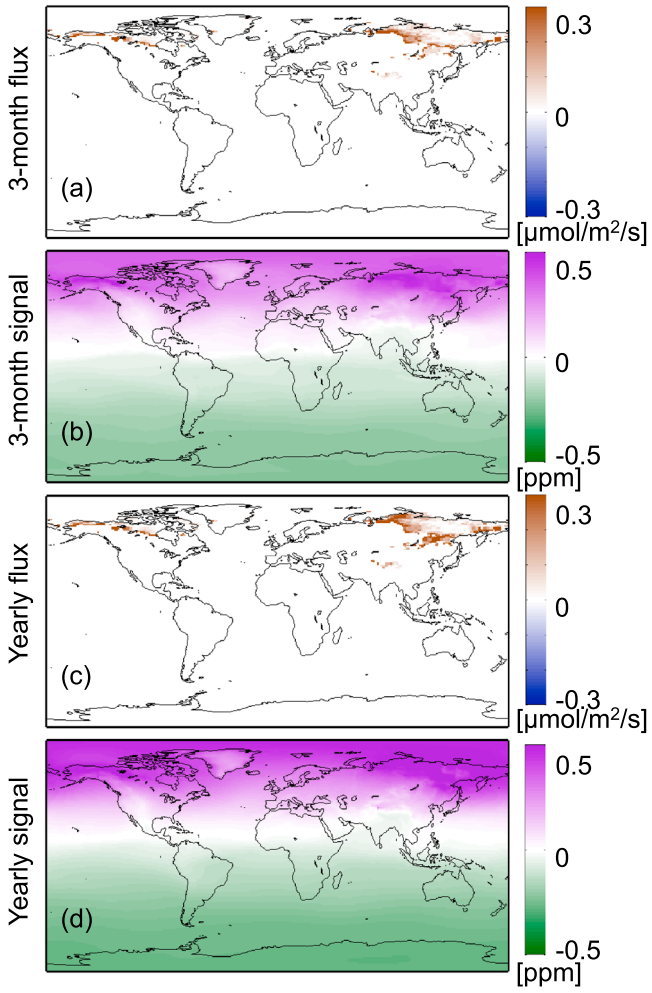

Figure 1. Flux and CO_2 concentrations for the permafrost carbon release experiment. (a) The 3 month average CO_2 flux ("3 month flux"), (b) 3 month average CO_2 concentration ("3 month signal"), (c) yearly average CO_2 flux ("yearly flux"), and (d) yearly average CO_2 concentration ("yearly signal"). The 3 month period is May through July. The flux is modeled for 2022. The negative concentration values in the southern hemisphere are a result of the global mean adjustment.

2.2. Perturbation Flux Scenarios

Three case studies are developed based on areas of interest within carbon cycle science that are directly relevant to the ASCENDS mission goals, namely, the detection of regional changes in fossil fuel emissions, high-latitude CO_2 fluxes, and changes in CO_2 fluxes in the Southern Ocean. They represent quantitatively plausible scenarios of changes in carbon fluxes, henceforth referred to as perturbation flux scenarios, that could occur by the early to mid-2020s, the planned launch time frame for ASCENDS. These scenarios are used as prototypical examples of flux patterns that give rise to the types of signals the ASCENDS mission endeavors to detect. The perturbation fluxes are added to the baseline fluxes within the PCTM modeling framework described in section 2.1 to produce the perturbation CO_2 atmospheres, henceforth referred to as perturbation runs.

2.2.1. Permafrost Carbon Release

The permafrost carbon feedback is an amplification of surface warming due to the release of CO_2 and methane from thawing permafrost [*Zimov et al.* 2006]. Permafrost soils in the high northern latitudes contain approximately 1700 Gt of carbon in the form of frozen organic matter [*Tarnocai et al.* 2009]. Permafrost is perennially frozen ground remaining at or below 0°C for at least two consecutive years [*Brown et al.* 1998], occupying about 24% of the exposed land area in the northern hemisphere [*Zhang et al.* 1999]. As temperatures increase in the future and the permafrost thaws, the organic material will also thaw and begin to decay, releasing CO_2 and methane into the atmosphere. CO_2 and methane emissions from thawing permafrost will amplify the warming due to anthropogenic greenhouse gas emissions [*Zimov et al.* 2006].

The permafrost carbon emission scenario applied here uses projections of CO_2 fluxes from thawing permafrost from *Schaefer et al.* [2011]. *Schaefer et al.* [2011] use the Simple Biosphere/Carnegie-Ames-Stanford approach land surface model [*Schaefer et al.*, 2008] driven by output from several general circulation models for the A1B scenario from the Intergovernmental Panel on Climate Change Fourth Assessment report [*Lemke et al.*, 2007]. The fluxes are an ensemble mean of 18 projections from 2002 to 2200. We ran the PCTM model with the extracted fluxes for 2020 to 2022 and used the 2022 fluxes as perturbation fluxes. The annual integrals for the permafrost perturbation fluxes are 0.613 PgC/yr, 0.641 PgC/yr, and 0.752 PgC/yr for 2020 to 2022, respectively.

The flux perturbations are concentrated in areas of discontinuous permafrost along the southern margins of permafrost regions (Figure 1). In discontinuous permafrost regions, north facing slopes might form permafrost, while south facing slopes may not. Permafrost temperatures hover just below freezing, making

these regions vulnerable to thaw for small increases in atmospheric temperature. Normally, the surface soils in the active layer thaw each summer and refreeze each winter. However, as temperatures increase, the thaw depth becomes too deep to refreeze in the winter, forming a talik or layer of unfrozen ground above the permafrost. The talik allows microbial decay to continue during winter when the surface soils are frozen, resulting in year-round fluxes that peak in summer when soil temperatures are highest (see Figure S1 in the supporting information).

The CO_2 concentrations of the baseline run were mean adjusted to match the annual mean of the perturbation run by applying a multiplicative adjustment. This adjustment preserves the spatial patterns of the baseline run, while the global difference in concentrations between the baseline and perturbation run is zero, so effectively, a global flux-neutral scenario. This has been done to focus this study on the detectability of changes in spatial patterns rather than detecting the mean interannual increase in CO_2 concentrations that results from the strictly positive perturbation fluxes over the 2 years of model spin-up and the investigated year.

2.2.2. Shift in Fossil Fuel Emissions

The fossil fuel flux perturbation scenario consists of a shift of fossil fuel emissions from Europe to China, a shift that is in directional agreement with recent trends in these regions. Fossil fuel emissions from China have increased rapidly over the last decades, and China is now the largest emitter of CO_2 worldwide [*Olivier et al*., 2012; *Peters et al*., 2011]. By comparison, fossil fuel emissions from Europe decreased 3% in 2011 relative to 2010 with an overall decline over the last two decades [*Olivier et al*., 2012]. We used two magnitudes of emission shift, from here on referred to as the "lower" and "higher" signals, representing two points on a continuum of possible emission changes around the year 2022.

The lower signal represents a 20% decrease of European emissions, with a 12% increase in China (Figure 2) that exactly offsets the European decrease. The higher signal includes a 50% decrease of emissions in Europe with a corresponding 30% increase in China (Figure 2) and is used for illustration purposes only as a decrease of this size is not expected in Europe within a decade. All the percentage changes are in reference to 2007 emission levels based on the v2011 2007 fossil fuel emissions from the CDIAC database [*Andres et al*., 2011]. The annual flux integrals for the lower and higher signals are 0.228 PgC/yr and 0.571 PgC/yr, respectively. We use these two shift settings as examples to draw broader conclusions on the detectability of these types of signals as characterized by their spatial and temporal patterns and their magnitudes.

The flux perturbations are globally flux neutral, in that European fossil fuel fluxes are reduced by a set percentage in each month and the total emissions from China are increased by the same mass amount. The decrease and increase are conducted proportionally to the existing spatial pattern of the fluxes for each month, thereby preserving the spatial and temporal patterns within the European and Chinese fluxes (Figures S2 and S3 in the supporting information). The fluxes vary relatively little from month to month, on average ±15%. Overall, the signal to be detected is a difference in the spatial distribution of CO_2 concentrations, with the global mean remaining unchanged.

2.2.3. Changes in Southern Ocean Fluxes

The Southern Ocean is of special interest to carbon cycle science, because its CO_2 fluxes are highly uncertain [*Gruber et al*., 2009]; it is a region with apparent high sensitivity to climate change [*Le Quéré et al*., 2009], and this sensitivity has implications for the region's future as a carbon sink, because half of the ocean uptake of anthropogenic CO_2 is estimated to occur there [e.g., *Le Quéré et al*., 2009; *Meredith et al*., 2012]. There is disagreement on the current and future trends of the carbon flux in the Southern Ocean [*Le Quéré et al*., 2009; *Law et al*., 2008b]. The Southern Ocean is also a very sparsely sampled region, where the ability of the ASCENDS mission to observe at high latitudes could provide valuable insights.

Variations in climate modes are a key driver of interannual variability in ocean carbon exchange [e.g., *Field et al*., 2007]. Here we evaluate the extent to which interannual variability due to variations in climatic modes, such as the El Niño–Southern Oscillation (ENSO), can be detected as a reference for addressing potential changes in the sink/source characteristics of the Southern Ocean using satellite observations. In other words, we use ENSO-related variability as a prototypical example of the scale of variability to detect. To that end, the years 1977 and 1979 were chosen as examples of estimated flux patterns as they represent large differences in ocean fluxes due to variations in climatic modes.

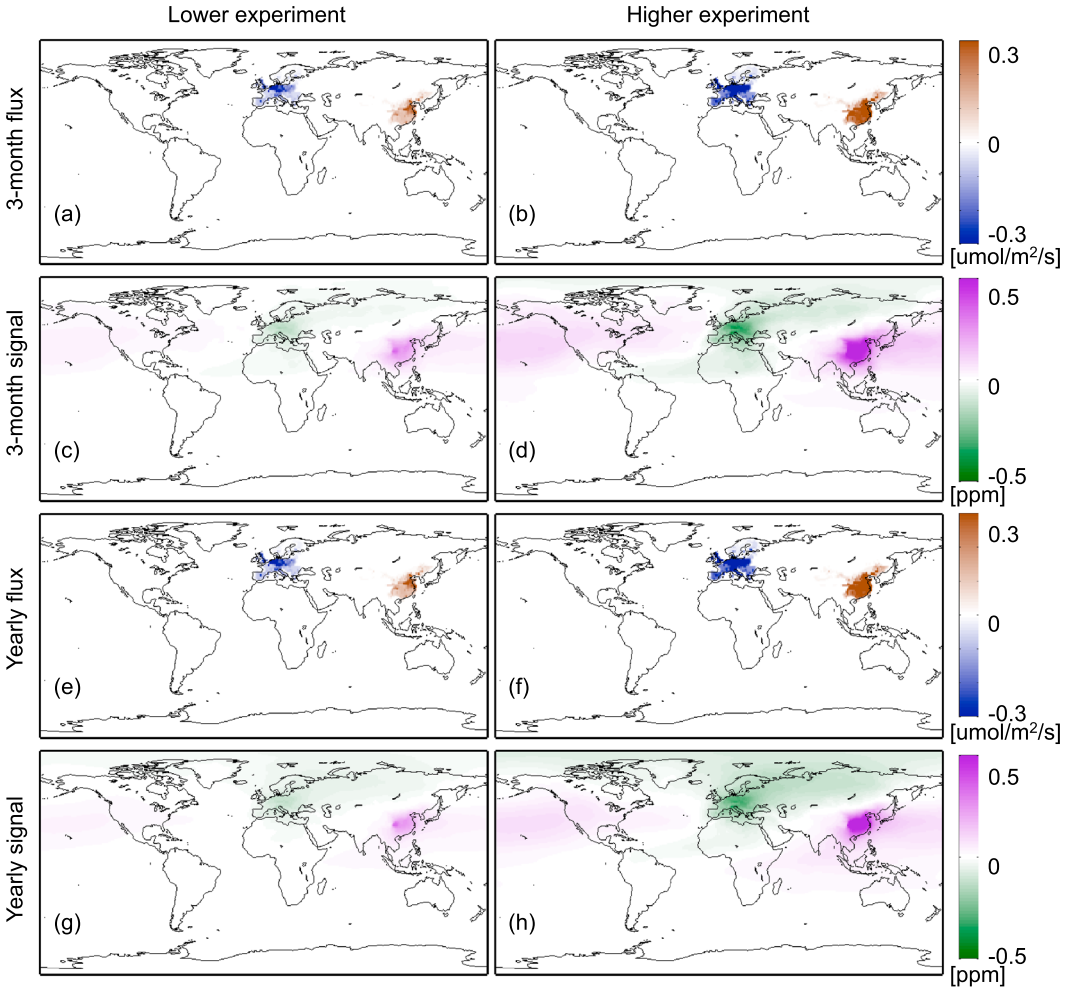

Figure 2. Flux and CO_2 concentrations for the fossil fuel experiments. (first row) The 3 month average CO_2 flux (3 month flux). (second row) The 3 month average CO_2 concentration (3 month signal). (third row) Yearly average CO_2 flux (yearly flux). (fourth row) Yearly average CO_2 concentration (yearly signal). The 3 month period is August through September.

The Southern Ocean fluxes for this scenario are based on a hindcast simulation of the Community Climate System Model Ocean Biogeochemical Elemental Cycle model as described by *Doney et al*. [2009]. The fluxes were obtained at 1°×1° spatial and monthly temporal resolution. The monthly difference between the Southern Ocean flux anomaly for 1977 and 1979 is used as the perturbation flux for this scenario. Figures 3a and 3c show the average flux perturbation for April through June and the full year, respectively. A year-round time series of these monthly perturbation fluxes is shown in Figure S4 in the supporting information. The magnitude of the perturbation fluxes (1977: 0.186 PgC/yr, 1979: −0.176 PgC/yr) is low relative to the other two case studies. In contrast to the other two experiments, the sign of the perturbation flux also varies by month and spatially within the region.

2.3. Simulated ASCENDS CO_2 Observations

Anticipated ASCENDS sampling and random measurement error characteristics are derived from model output and observations in a method similar to that of *Kawa et al*. [2010] and *Kiemle at al*. [2014]. The Cloud-Aerosol Lidar and Infrared Pathfinder Satellite Observation (CALIPSO) orbital track is used to simulate the expected ASCENDS sampling. Synthetic observations are sampled from model output at the nearest time to the satellite overflight and interpolated in space to the CALIPSO sample locations. A vertical weighting function, appropriate to an ASCENDS laser instrument operating at a wavelength near 1.57 μm, is applied to the model pseudodata profile to produce column average mixing ratio values [*Ehret et al*., 2008]. We consider only random errors due to photon counting. Potential bias errors [e.g., *Baker et al*., 2010], which could

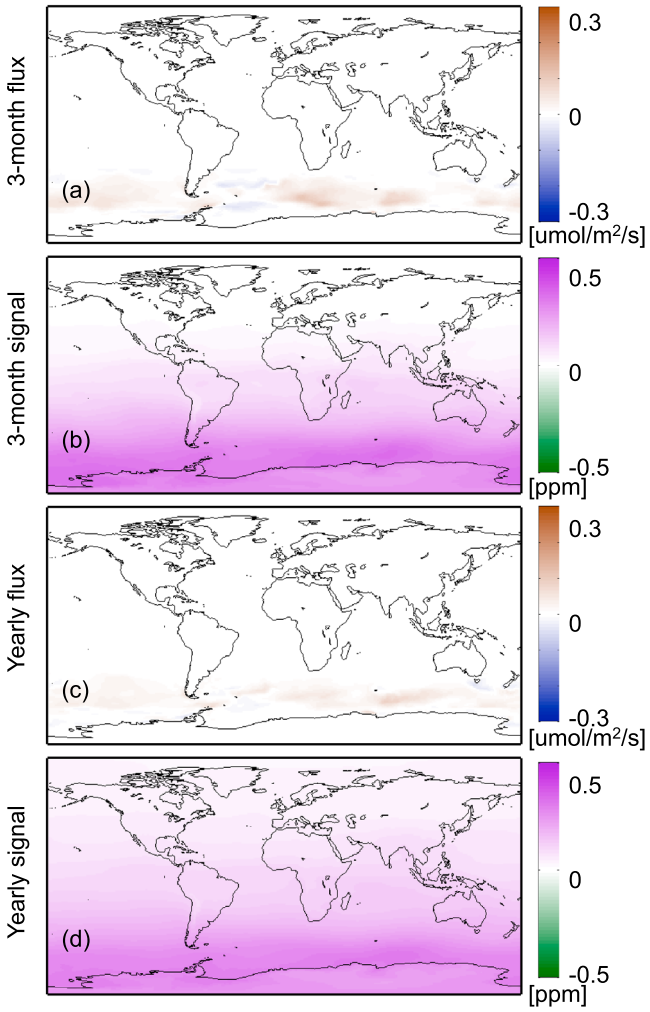

Figure 3. Flux and CO_2 concentrations for the Southern Ocean experiment. (a) The 3 month average CO_2 flux (3 month flux), (b) 3 month average CO_2 concentration (3 month signal), (c) yearly average CO_2 flux (yearly flux), and (d) yearly average CO_2 concentration (yearly signal). The 3 month period is April through June.

significantly complicate the analysis if correlated with geophysical variables of interest (e.g., land/ocean or vegetation cover), are not included.

CALIPSO measurements of total cloud and aerosol optical depth (OD) are used to calculate the ASCENDS laser attenuation. CALIPSO OD data are reported every 5 km (corresponding to every 0.7435 s) along track, and this forms the basic ASCENDS sample set. Surface lidar backscatter (β), also needed for error estimation, follows from MODIS-measured spectral reflectance over land and the glint formulation of *Hu et al*. [2008] over water using daily MERRA 10 m wind speeds. Surface reflectivity over land is interpolated from MODIS (Terra + Aqua) 5 km 16 day composite nadir bidirectional reflectance distribution function-adjusted reflectance data (α) at 1.64 μm (band 6), which are available every 8 days [*Schaaf et al*., 2002]. Land reflectance is scaled by a factor of 1.23 to account for the land "hot spot" backscatter effect [*Disney et al*., 2009], i.e., $\beta\ (\mathrm{sr}^{-1}) = 1.23\,\alpha/\pi$. Backscatter values of 0.08 sr^{-1} and 0.01 sr^{-1} are used to fill missing areas of MODIS data over land and over snow/ice, respectively, where ice and snow cover are determined from MERRA data.

In order to make our study method applicable for a range of possible CO_2 laser sounder instrument implementations, we scale the errors globally to a nominal error value for clear-air conditions at Railroad Valley, Nevada ($\beta = 0.176$, $T = 1$) and a 10 s (67.2 km) sample integration. Thus, a given instrument model can be characterized by its random error at the Railroad Valley reference point and the global distribution of errors estimated from OD and β. The individual sounding errors at the 5 km CALIPSO resolution are calculated using

$$\sigma_{5\mathrm{km}} = \frac{3.667\sigma_{\mathrm{ref}}}{\sqrt{\beta T^2 f / 0.176}} \tag{1}$$

where σ_{ref} is the 10 s reference instrument random error (standard deviation) at Rail Road Valley, T is the transmittance, f is the surface detection frequency, and 0.176 is the Railroad Valley backscatter reference value at 1.57 μm, which corresponds to one of the potential ASCENDS instrument designs [*Abshire et al*., 2010]. The transmittance is calculated from the CALIPSO (OD) using $T = e^{-\mathrm{OD}}$.

Soundings with an optical depth greater than 0.3 or where the surface detection frequency equals zero are filtered out and considered "not retrieved." The surface detection frequency equals zero when none of the 1 km averaged CALIPSO samples in a 5 km average can see a ground return; i.e., the clouds/aerosol were too thick to get a return from the ground. For this study, we used a 10 s along-track average as our pseudodata measurement granule [*Kawa et al*., 2010]. Using this setup, the maximum number of soundings constituting one

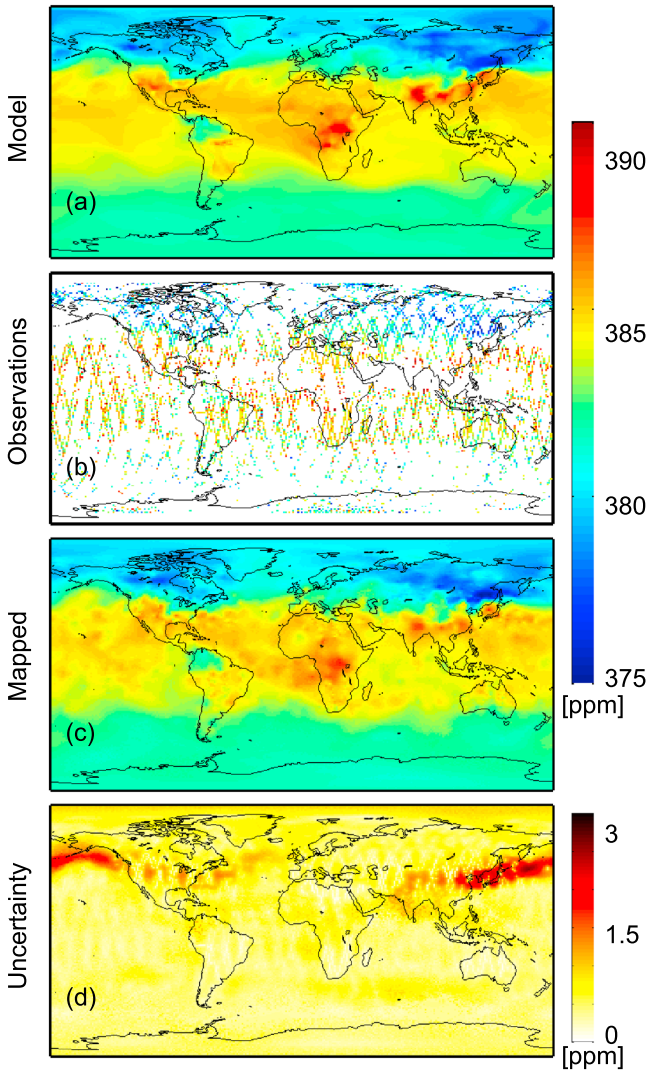

Figure 4. Mapping results for 1–4 August 2007. (a) Modeled CO_2 concentrations ("model"), (b) simulated ASCENDS observations ("observations"), (c) mapped CO_2 concentrations ("mapped"), and (d) mapping uncertainties ("uncertainty") expressed as a standard deviation.

observation is 14. The 10 s observation error variances are then calculated by averaging the 5 km error variances within each 10 s time interval and dividing this average by the number of retrieved soundings. This setup implies the assumption that retrieval errors between individual soundings are spatially and temporally uncorrelated. We include three measurement noise settings in the study. A no-measurement noise setting for reference purposes, and medium and high noise settings, which use Rail Road Valley 10 s reference instrument random errors (σ_{ref}) of 0.5 and 1 ppm, respectively. Once the measurement error variance has been determined for each location following the procedure described above, a random sample from a normal distribution with that variance is drawn and added to the PCTM model CO_2 value to define a pseudodata observation. The global mean errors (σ_{obs}) are 2.1 and 4.2 ppm, respectively, for the medium and high noise settings. Figure 4b provides an example of 4 days of global observations. Different random seed numbers are used for the errors in the baseline and the perturbation runs.

3. Methods

3.1. Mapping Approach

We use a geostatistical mapping approach [*Hammerling et al.*, 2012a, 2012b] to create contiguous interpolated maps, i.e., global mapped ("level 3") products for the comparison. Satellite CO_2 observations contain large gaps and high measurement errors such that meaningful spatially comprehensive comparisons at synoptic time scales are often precluded using the observations directly. Using gap-filled products makes it possible to conduct synoptic, global comparisons. The approach presented in *Hammerling et al.* [2012a, 2012b] also yields spatially explicit uncertainties (equation (7) in *Hammerling et al.* [2012a]) of the mapped products. These may be lower than the uncertainties of the individual observations in areas where the correlation with nearby observations can be leveraged, which in turn can facilitate signal detection.

The applied mapping methodology yields global mapped CO_2 concentrations with uncertainty measures without invoking assumptions about fluxes or atmospheric transport. The method leverages the spatial correlation in the atmospheric CO_2 concentration field, parameterized as an exponential covariance function with spatially varying variance and correlation range parameters using a moving window circular domain of 2000 km. These parameters are estimated from the observations and thus not imposed a priori. Methodological details are given in *Hammerling et al.* [2012a, 2012b].

Specific to this study, we filter the pseudodata observations to those with a measurement error standard deviation below a certain threshold. This is analogous to imposing a quality criterion when delivering remote

sensing data instead of making all retrievals available. For the medium (high) measurement error setup, this threshold is 1.5 (3.0) ppm. This choice represents a balance between spatial coverage and robustness of the covariance estimation procedure and was determined in a sensitivity analysis (results not shown). For the "no error" setup, which is only used as a theoretical best case, we use observations at the same locations as for the medium and high measurement setups, but without any noise added. We include this case to isolate any potential limitations of the methodology and the spatial coverage from those related to the instrument capabilities.

Mapping CO_2 satellite observations at synoptic time scales makes it possible to capture the dynamic behavior of CO_2 in the atmosphere [*Hammerling et al.*, 2012a, 2012b]. Based on preliminary studies evaluating mapping performance for different time periods, 4 day periods were found to provide the best balance between ensuring good data coverage while also capturing synoptic behavior for ASCENDS-like observations. Figure 4 shows an example of a 4 day (1–4 August 2007) period. The average modeled CO_2 distribution is shown for reference, and only the observations are used in the subsequent mapping procedure. Each 4 day period is mapped independently from other 4 day periods and for the baseline and perturbation runs. For January, only six 4 day periods were mapped due to missing CALIPSO data; for all other months, seven 4 day periods were mapped for a total of 83 4 day maps for each of the baseline and perturbation cases. These mapped fields were then used as input data in the subsequent comparison analysis described in section 3.2.

3.2. Comparison Approach

The detectability of a signal is assessed pointwise for each model grid cell by comparing the mapped concentrations from the baseline run and the perturbation run and determining whether the observed differences exceed their associated uncertainties. The uncertainty of the difference between two mapped concentration fields, expressed as a variance, is the sum of the estimation variances of the baseline, $\sigma^2_{\hat{y}_{base}}$, and the perturbation, $\sigma^2_{\hat{y}_{per}}$, mapped products

$$\sigma^2_{diff} = \sigma^2_{\hat{y}_{base}} + \sigma^2_{\hat{y}_{per}} \tag{2}$$

For ease of interpretation and visualization purposes, the comparison results are binned by their relative uncertainties, where the absolute value of the difference exceeds one, two, or three standard deviations, respectively, of the uncertainty of the difference.

Due to the measurement error added to the observations, together with the sparseness of the available observations, individual 4 day maps do not exhibit detectable differences in a statistical sense, and the question then becomes to identify a time period over which such 4 day maps must be averaged before a significant signal emerges. Under the assumption of temporal independence, the uncertainty (expressed as a variance) of the temporal mean is the mean mapping variance of the individual periods divided by the number of periods. The assumption of temporal independence was evaluated by conducting temporal variogram analyses for sets of mapping errors at randomly selected locations (results not shown), and no compelling indication to contradict this assumption was found.

4. Results and Discussion

On a high level, one can view the query of detecting atmospheric CO_2 concentration signals resulting from flux perturbations as two distinct, if connected, questions. The first question is how the characteristics of the flux perturbations are translated to, and preserved in, the atmospheric CO_2 concentrations; i.e., what is the signature (or signal) of a set of flux perturbations of interest in the atmospheric CO_2 concentrations. The second question is how well a given observing system, in our case, the ASCENDS mission, can capture the presence of this signal. Both of these aspects are discussed in the following sections, which are organized by the three investigated scenarios.

4.1. Detectability of Permafrost Carbon Release

A significant signal can be detected in the case of the anticipated permafrost carbon emissions (Figure 5 and Figure S5 in the supporting information). The challenge is in capturing longitudinal and latitudinal gradients, which can better attribute the increase to the permafrost region, as opposed to just detecting a zonal increase.

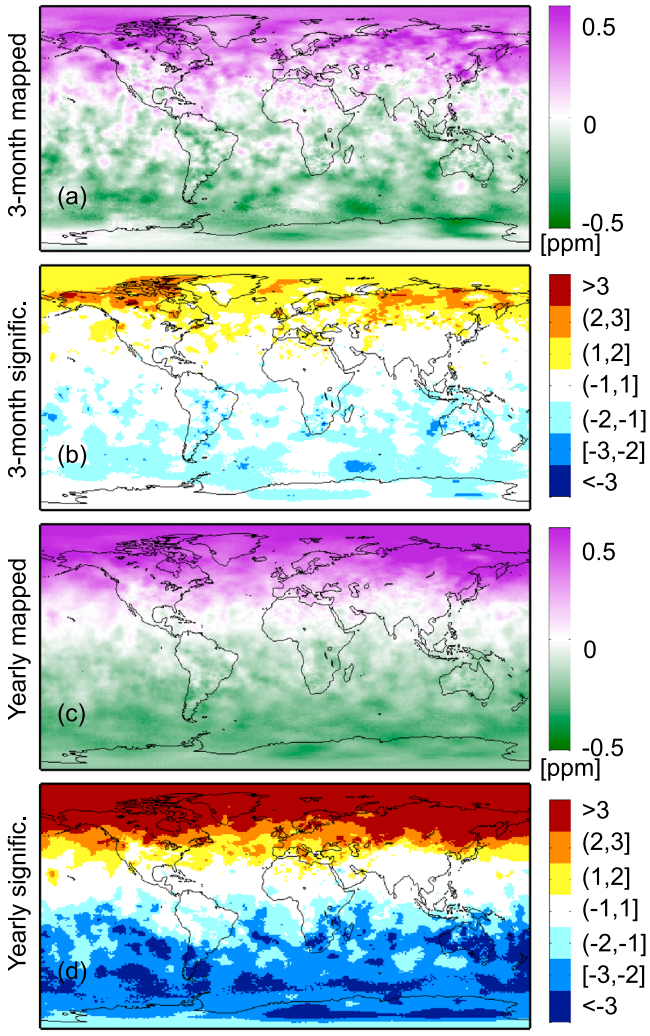

Figure 5. Results for the permafrost carbon release experiment for medium measurement noise. (a) The 3 month mapped CO_2 signal ("3 month mapped"), (b) significance of the 3 month mapped CO_2 signal ("3 month signific"), (c) yearly mapped CO_2 signal ("yearly mapped"), and (d) significance of the yearly mapped CO_2 signal ("yearly signific"). The mapped signal is the difference between the mapped perturbation CO_2 concentration and the mapped baseline CO_2 concentration. The significance is the mapped signal divided by the uncertainty of the mapped signal. The values are discretized for improved visualization. The yellow, orange, and dark red (light, medium, and dark blue) represent areas where the mapped perturbation concentration is larger (smaller) than the mapped baseline concentration by more than one, two, or three standard deviations, respectively, of the uncertainty of the mapped signal. The 3 month period is May through July.

While signal detection is not directly targeted at quantifying carbon fluxes, insights on the detectability of spatial gradients are highly relevant for studies targeting flux detections, e.g., atmospheric inverse modeling studies. With this in mind, a judicious choice of the temporal aggregation periods over which the comparisons are conducted is important.

Because of the seasonality of the fluxes in the permafrost carbon release scenario (Figure S1 in the supporting information), the gradients in the atmospheric CO_2 distribution are most evident in the months following the start of the spring thaw. As a result, averaging over spring/summer months yields a clearer identification of the geographic origin of the signal relative to aggregating maps over the full year. While the concentration signal is highest around September (Figure S1 in the supporting information), or even later in the year, when the active layer is deepest, the concentration signals indicative of the spatial pattern of the tundra fluxes are most distinct in the late spring/early summer months before the effects of atmospheric mixing take over. By August, atmospheric mixing, which occurs rapidly in the Arctic, causes the spatial signature of the tundra melting fluxes to be replaced by the dominant signal of a zonal increase. Some further evidence of this phenomenon can be observed by comparing Figures 1b and 1d: the 3 month signal retains more of the spatial characteristics, whereas the yearly signal represents a zonal increase where the elevated concentrations have spread toward the pole. This phenomenon is caused by the specific combination of the temporal pattern of the permafrost carbon release and rapid atmospheric mixing in the high northern latitudes.

Figure 5 and Figure S5 in the supporting information show a summary of the detection results for the permafrost carbon release scenario. While the 3 month results feature comparatively more noise, the recognition of the spatial pattern in the significance plots is also improved. Even for the high-noise scenario, the land origin of the signal is better seen in the 3 month maps relative to the yearly plots. The results for the different noise levels are as expected; lower noise provides a more accurate mapped concentration field (Figure S5 in the supporting information). Overall, the permafrost CO_2 perturbation is detectable for both levels of measurement noise considered, and spatial gradients are best detected using 2 to 3 month aggregation periods in the late spring/early summer.

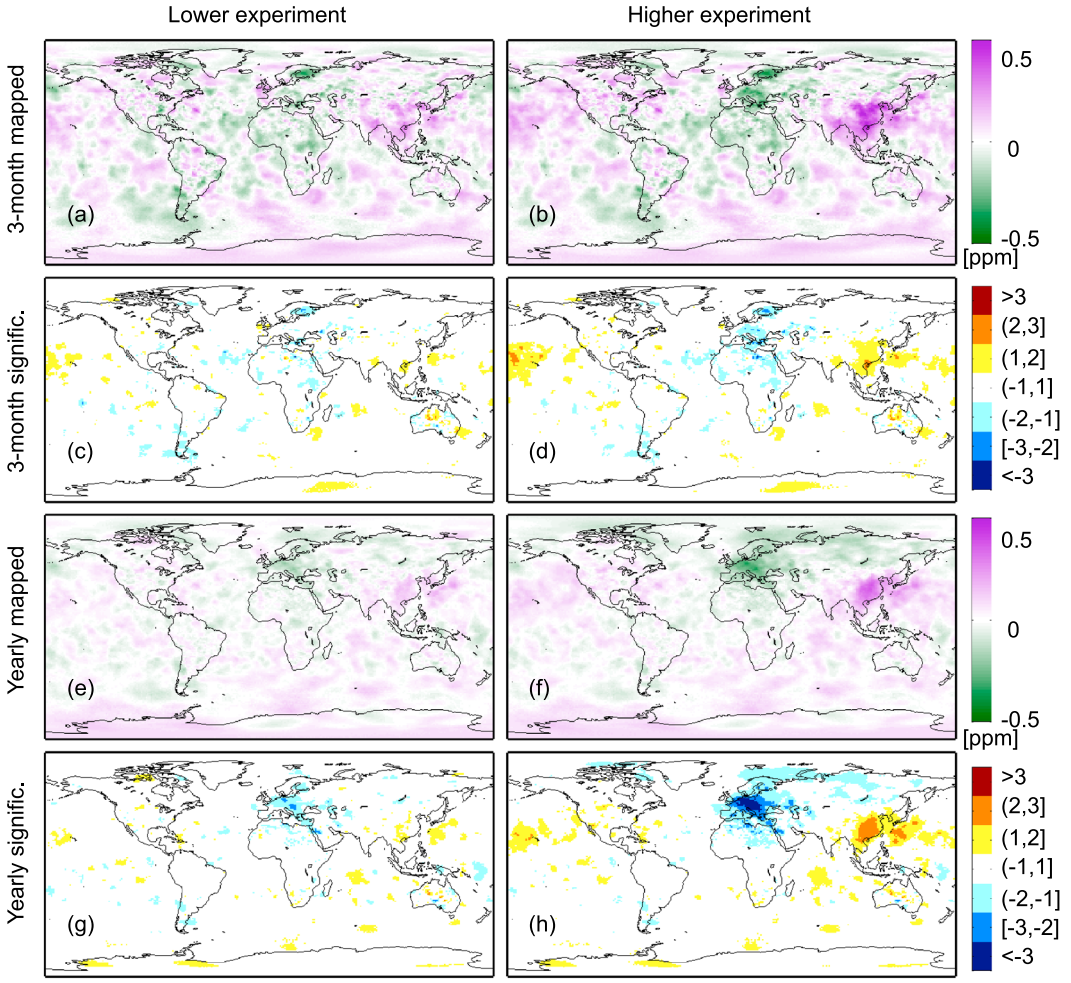

Figure 6. Results for the fossil fuel experiments for medium measurement noise. (first row) The 3 month mapped CO_2 signal (3 month mapped). (second row) The significance of the 3 month mapped CO_2 signal (3 month signific). (third row) The yearly mapped CO_2 signal (yearly mapped). (fourth row) The significance of the yearly mapped CO_2 signal (yearly signific). The mapped signal is the difference between the mapped perturbation CO_2 concentration and the mapped baseline CO_2 concentration. The significance is the mapped signal divided by the uncertainty of the mapped signal. The values are discretized for improved visualization. The yellow, orange, and dark red (light, medium, and dark blue) represent areas where the mapped perturbation concentration is larger (smaller) than the mapped baseline concentration by more than one, two, or three standard deviations, respectively, of the uncertainty of the mapped signal. The 3 month period is August through September.

4.2. Detectability of Shift in Fossil Fuel Emissions

The examined fossil fuel emission perturbations lead to a pronounced spatial signature that is localized over Europe and China (Figures 2c, 2g, 2d, and 2h and Figures S2 and S3 in the supporting information). This is in contrast to the other two experiments (see Figures 1d and 3d), where the detailed spatial signatures are largely lost and especially the yearly signals represent primarily zonal increases. In addition, the magnitude of the lower fossil fuel perturbation signal is very low, which, combined with its small spatial extent, renders the weak fossil fuel signal the most difficult to detect among the investigated scenarios. This exemplifies the challenge of detecting small and localized flux changes from satellite observations.

The highly localized nature of the signal over Europe and China suggests that changes in fluxes would be detectable and attributable to a given region even if these fluxes were not offset by a corresponding shift in emissions within a similar latitudinal range. It is interesting to observe the different dispersion patterns of the European and Chinese emissions, especially when considering their latitudinal range. The effect on the atmospheric concentrations of the European emissions can be observed from equatorial Africa to the Arctic, whereas the range of the Chinese emissions is more limited to their originating latitudinal band (see Figure 2h).

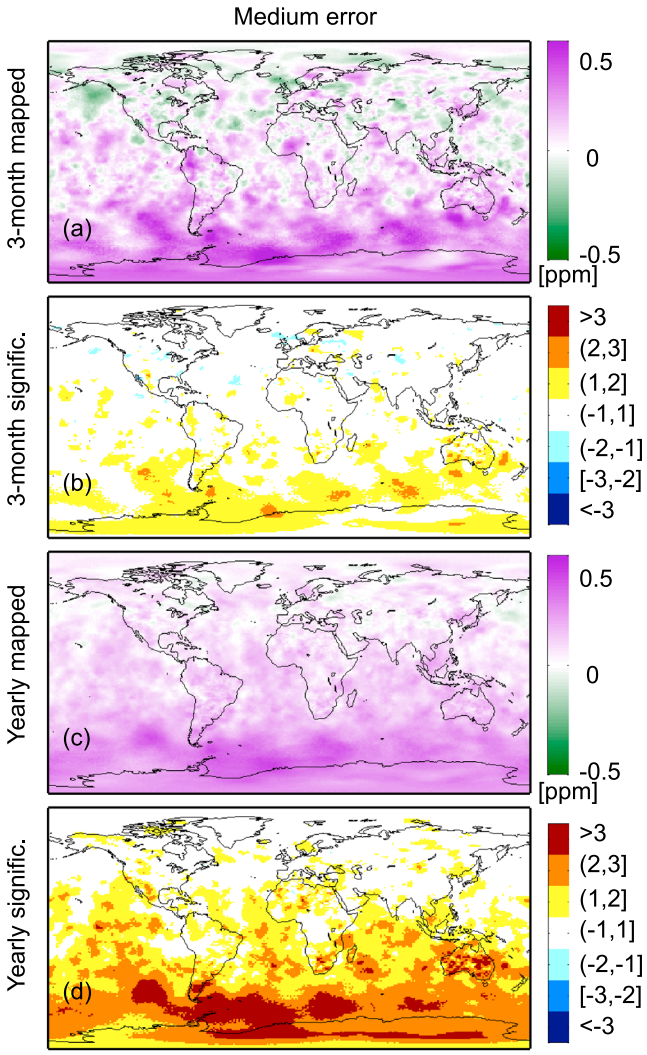

Figure 7. Results for the Southern Ocean experiment for medium measurement noise. (a) The 3 month mapped CO_2 signal (3 month mapped), (b) significance of the 3 month mapped CO_2 signal (3 month signific), (c) yearly mapped CO_2 signal (yearly mapped), and (d) significance of the yearly mapped CO_2 signal (yearly signific). The mapped signal is the difference between the mapped perturbation CO_2 concentration and the mapped baseline CO_2 concentration. The significance is the mapped signal divided by the uncertainty of the mapped signal. The values are discretized for improved visualization. The yellow, orange, and dark red (light, medium, and dark blue) represent areas where the mapped perturbation concentration is larger (smaller) than the mapped baseline concentration by more than one, two, or three standard deviations, respectively, of the uncertainty of the mapped signal. The 3 month period is April through June.

Given the relative lack of seasonality in the fossil fuel perturbation scenarios, averaging over longer periods of time leads to better detectability (Figure 6). Although atmospheric transport clearly plays a role, the atmospheric signal remains indicative of the source region of the perturbation flux throughout the seasons. Figure 6h, for example, shows evidence that both the source and downwind regions of the emissions have a significant signature in the atmosphere.

The effect of varying measurement noise levels on the detectability is again as expected; increasing measurement noise leads to decreased significance in the results and requires in turn longer averaging periods. For the higher signal, all three noise levels capture the signal in the yearly results, which is not the case for the lower signal, where only the no error case clearly captures the signal (Figure S6 in the supporting information). There is some evidence that a significant signal is detectable in the yearly medium and high-error measurement noise cases (Figure 6), and given the nature of the signal discussed above, the signal is expected to appear more clearly when averaging over periods exceeding 1 year. Overall, these findings imply that ASCENDS can in principle detect anthropogenic signal components, but depending on the strength of the signal, detection might require multiple years. It is hence feasible that ASCENDS can serve to validate anthropogenic emission changes over the course of its mission but is likely not ideal as the primary monitoring tool for such flux changes.

4.3. Detectability of Changes in Southern Ocean Fluxes

The detection of changes in the Southern Ocean source/sink characteristics is challenging as a result of a confluence of different factors. The overall magnitude of the signal in the Southern Oceans is rather weak, with the absolute value of the signal never exceeding 0.4 ppm in the column. In addition, this scenario involves subseasonal and subregional scale flux variability that is superimposed on a seasonal pattern in the fluxes (Figure S4 in the supporting information). Atmospheric mixing also plays a role insofar as it obscures the Southern Ocean as the origin of the signal as was also observed in the permafrost carbon release scenario. However, applying the remedy of using a shorter averaging period before atmospheric mixing hides the origin of the signal is not as clear-cut for the Southern Ocean scenario, because the overall signal is weaker. Spatial gradients associated with the

Southern Ocean flux perturbation are most evident in the spring and early summer (Figure 3). Later in the year, although the concentration signal is stronger, the concentration increase has spread poleward and is less attributable to the Southern Ocean.

For all measurement noise setups, the yearly results clearly indicate a zonal increase in the high southern latitudes (Figure 7 and Figure S8 in the supporting information). However, it is less clear whether the pattern is indicative of the Southern Ocean being the source region within the zonal band. The spatial pattern of the 3 month results (Figure 7b) is more indicative of the Southern Ocean as the source region, but the significance levels are not very high. The most beneficial approach for the Southern Ocean scenario appears to be conducting analyses over periods of multiple lengths and drawing conclusions from the joint picture emerging from these analyses. In summary, ASCENDS can detect a Southern Ocean signal representative of differences due to natural variability in the ENSO climatic mode. ASCENDS may provide a unique measurement view of these regions because the pervasive cloudiness and low sun angles present difficult conditions for passive satellite CO_2 sensors. Due to the low-magnitude and small-scale variability within the fluxes giving rise to the signal, however, attributing the signal to specific ocean regions or biogeophysical processes will likely require additional corroborative information.

5. Conclusions

This work assesses the degree to which ASCENDS, a planned lidar CO_2 observing satellite mission, can contribute to the detection of three types of CO_2 flux change scenarios relevant to global carbon cycle science: the release of carbon due to the thawing of permafrost in the northern high latitudes, the shifting of fossil fuel emissions from Europe to China, and ENSO-related changes in the source/sink characteristics in the Southern Ocean. These three scenarios were used to design OSSEs for signal detection studies to investigate if the ASCENDS mission has the ability to detect the unfolding of these scenarios compared to a baseline scenario. Two different levels of measurement noise and a no-measurement noise reference cases were investigated.

This study is based on a number of simplifications. For each scenario, the only flux component that is varied is the flux component under investigation, while all other fluxes are fixed. In reality, many changes might occur simultaneously, and the resulting CO_2 concentration signal patterns might overlap, which makes signal detection more challenging. We have introduced some additional variability by sampling and mapping the baseline concentration field rather than assuming a static baseline concentration field in the comparison procedure, however, that might not be equivalent to, for example, having misspecified biospheric fluxes. Such misspecifications could be aliased with the true signals and misleading signal patterns could occur. This could impact the conclusions of this study insofar that it would be more difficult to link detectable signals with the underlying change in fluxes.

The results indicate that the ASCENDS mission can in principle detect the types of signals investigated in this study. The permafrost thawing flux perturbation is readily detectable at a high level of significance. Spatial gradients, which are of great interest for process attribution, were best detected using 2 or 3 month aggregation periods in the late spring/early summer. For the Southern Ocean scenario, differences due to the natural variability in the ENSO climatic mode were primarily detectable as a zonal increase. The relative magnitude of the signal, however, is much smaller than the permafrost-thawing signal. Spatial and temporal high-frequency changes in the anomaly fluxes produce additional variability in the signal, making detection of more detailed gradients than a zonal increase challenging for the Southern Ocean scenario. Conducting analyses over periods of varying lengths and analyzing them jointly provide a possible diagnostic strategy.

The fossil fuel emission detectability is directly related to the strength of the signal and the level of measurement noise. As is true for all scenarios, the effect of varying measurement noise levels is as expected: increasing measurement noise levels leads to decreased significance in the results and requires in turn longer averaging periods. For the nominal (lower) fossil fuel emission signal, only the noise-free instrument test produces a clearly detectable signal, while all three noise levels capture the higher (exaggerated) signal case. The emergence of a detectable signal suggests that averaging over periods longer than the 1 year period considered in this study would also render signals of the magnitude of the lower fossil fuel emission signal detectable.

All in all, the expected precision and sampling characteristics of ASCENDS promise to substantially enhance our ability to detect variations in CO_2 fluxes and to inform the mechanisms that control them. Future work includes comparing the signal detection performance of ASCENDS to passive sensors, which might be employed within the time frame of the ASCENDS mission. Additional future work entails a comprehensive study of the effect of uncertainties in fluxes other than those defining the signal on the detectability of the signal, for example, by using an ensemble of biospheric fluxes to vary the baseline fluxes.

Acknowledgments

This material is based upon work supported by the National Aeronautics and Space Administration under grant NNX08AJ92G issued through the Research Opportunities in Space and Earth Sciences Carbon Cycle Science program and by Jet Propulsion Laboratory subcontract 1442785 as well as the ASCENDS Science Requirements Definition Team. S. Doney acknowledges support from U.S. National Science Foundation (AGS-1048827). K. Schaefer acknowledges support from the National Oceanic and Atmospheric Administration under grant NA09OAR4310063 and from the National Aeronautics and Space Administration under grant NNX10AR63G. All the data used in this study can be requested by emailing Dorit Hammerling (dorith@ucar.edu). We thank Robert Andres for providing CDIAC fossil fuel emission fluxes and his advice in applying them. We thank Ivan Lima for his support with the Southern Ocean fluxes and Michael Manyin and Yuping Liu for executing PCTM model runs.

References

Abshire, J. B., H. Riris, G. R. Allan, C. J. Weaver, J. Mao, X. Sun, W. E. Hasselbrack, S. R. Kawa, and S. Biraud (2010), Pulsed airborne lidar measurements of atmospheric CO_2 column absorption, *Tellus B*, *62*, 770–783, doi:10.1111/j.1600-0889.2010.00502.x.

Andres, R. J., T. A. Boden, and G. Marland (2009), Monthly Fossil-Fuel CO_2 Emissions: Mass of Emissions Gridded by One Degree Latitude by One Degree Longitude, Carbon Dioxide Information Analysis Center, Environmental Sciences Division, Oak Ridge National Laboratory, Oak Ridge, Tenn., 37831-6290.

Andres, R. J., J. S. Gregg, L. Losey, G. Marland, and T. A. Boden (2011), Monthly, global emissions of carbon dioxide from fossil fuel consumption, *Tellus B*, *63*, 309–327, doi:10.1111/j.1600-0889.2011.00530.x.

ASCENDS Workshop Steering Committee (2008), Active Sensing of CO_2 Emissions over Nights, Days, and Seasons (ASCENDS) Mission NASA Science Definition and Planning Workshop Report, 1–78.

Baker, D. F., H. Bösch, S. C. Doney, D. O'Brien, and D. S. Schimel (2010), Carbon source/sink information provided by column CO_2 measurements from the orbiting carbon observatory, *Atmos. Chem. Phys.*, *10*, 4145–4165, doi:10.5194/acp-10-4145-2010.

Bian, H., S. R. Kawa, M. Chin, S. Pawson, Z. Zhu, P. Rasch, and S. Wu (2006), A test of sensitivity to convective transport in a global atmospheric CO_2 simulation, *Tellus B*, *58*, 463–475, doi:10.1111/j.1600-0889.2006.00212.x.

Brown, J., O. J. Ferrians Jr., J. A. Heginbottom, and E. S. Melnikov (1998), Circum-arctic map of permafrost and ground ice conditions, Natl. Snow and Ice Data Cent., Digital media, Boulder, Colo. [Revised February 2001.]

Canadell, J. G., C. L. Quéré, M. R. Raupach, C. B. Field, E. T. Buitenhuis, P. Ciais, T. J. Conway, N. P. Gillett, R. A. Houghton, and G. Marland (2010), Carbon sciences for a new world, *Curr. Opin. Environ. Sustainability*, *2*.

Chatterjee, A., A. M. Michalak, J. L. Anderson, K. L. Mueller, and V. Yadav (2012), Toward reliable ensemble Kalman filter estimates of CO_2 fluxes, *J. Geophys. Res.*, *117*, D22306, doi:10.1029/2012JD018176.

Crisp, D., et al. (2004), The Orbiting Carbon Observatory (OCO) mission, *Adv. Space Res.*, *34*, 700–709, doi:10.1016/j.asr.2003.08.062.

Disney, M. I., P. E. Lewis, M. Bouvet, A. Prieto-Blanco, and S. Hancock (2009), Quantifying surface reflectivity for spaceborne lidar via two independent methods, *IEEE Trans. Geosci. Remote Sens.*, *47*, 3262–3271.

Doney, S. C., I. Lima, R. A. Feely, D. M. Glover, K. Lindsay, N. Mahowald, J. K. Moore, and R. Wanninkhof (2009), Mechanisms governing interannual variability in upper-ocean inorganic carbon system and air-sea CO_2 fluxes: Physical climate and atmospheric dust, *Deep Sea Res., Part II*, *56*(8–10), 640–655, doi:10.1016/j.dsr2.2008.12.006.

Ehret, G., C. Kiemle, M. Wirth, A. Amediek, A. Fix, and S. Houweling (2008), Space-borne remote sensing of CO_2, CH_4, and N_2O by integrated path differential absorption lidar: A sensitivity analysis, *Appl. Phys. B*, *90*, 593–608, doi:10.1007/s00340-007-2892-3.

Field, C. B., J. Sarmiento, and B. Hales (2007), The carbon cycle of North America in a global context, in *The First State of the Carbon Cycle Report (SOCCR): The North American Carbon Budget and Implications for the Global Carbon Cycle. A Report by the U.S. Climate Change Science Program and the Subcommittee on Global Change Research*, edited by A. W. King et al., pp. 21–28, Natl. Oceanic and Atmos. Admin., Natl. Clim. Data Cent., Asheville, N. C.

Gruber, N., et al. (2009), Oceanic sources, sinks, and transport of atmospheric CO_2, *Global Biogeochem. Cycles*, *23*, GB1005, doi:10.1029/2008GB003349.

Hammerling, D. M., A. M. Michalak, and S. R. Kawa (2012a), Mapping of CO_2 at high spatiotemporal resolution using satellite observations: Global distributions from OCO-2, *J. Geophys. Res.*, *117*, D06306, doi:10.1029/2011JD017015.

Hammerling, D. M., A. M. Michalak, C. O'Dell, and S. R. Kawa (2012b), Global CO_2 distributions over land from the Greenhouse Gases Observing Satellite (GOSAT), *Geophys. Res. Lett.*, *39*, L08804, doi:10.1029/2012GL051203.

Hu, Y., et al. (2008), Sea surface wind speed estimation from space-based lidar measurements, *Atmos. Chem. Phys.*, *8*, 3593–3601, doi:10.5194/acp-8-3593-2008.

Kawa, S. R., D. J. Erickson III, S. Pawson, and Z. Zhu (2004), Global CO_2 transport simulations using meteorological data from the NASA data assimilation system, *J. Geophys. Res.*, *109*, D18312, doi:10.1029/2004JD004554.

Kawa, S. R., J. Mao, J. B. Abshire, G. J. Collatz, X. Sun, and C. J. Weaver (2010), Simulation studies for a space-based CO_2 lidar mission, *Tellus B*, *62*, 759–769, doi:10.1111/j.1600-0889.2010.00486.x.

Kiemle, C., S. R. Kawa, M. Quatrevalet, and E. V. Browell (2014), Performance simulations for a spaceborne methane lidar mission, *J. Geophys. Res. Atmos.*, *119*, 4365–4379, doi:10.1002/2013JD021253.

Kuze, A., H. Suto, M. Nakajima, and T. Hamazaki (2009), Thermal and near infrared sensor for carbon observation Fourier-transform spectrometer on the greenhouse gases observing satellite for greenhouse gases monitoring, *Appl. Opt.*, *48*, 6716–6733, doi:10.1364/AO.48.006716.

Law, R. M., et al. (2008a), TransCom model simulations of hourly atmospheric CO_2: Experimental overview and diurnal cycle results for 2002, *Global Biogeochem. Cycles*, *22*, GB3009, doi:10.1029/2007GB003050.

Law, R. M., R. J. Matear, and R. J. Francey (2008b), Comment on saturation of the Southern ocean CO_2 sink due to recent climate change, *Science*, *319*, 570.

Le Quéré, C., M. R. Raupach, J. G. Canadell, and E. A. Marland (2009), Trends in the sources and sinks of carbon dioxide, *Nat. Geosci.*, *2*, 831–836.

Lemke, P., et al. (2007), Changes in snow, ice and frozen ground, in *Climate Change 2007: The Physical Science Basis: Contribution of Working Group I to the Fourth Assessment Report of the Intergovernmental Panel on Climate Change*, edited by S. Solomon et al., Cambridge Univ. Press, Cambridge, U. K.

Mao, J., and S. R. Kawa (2004), Sensitivity studies for space-based measurement of atmospheric total column carbon dioxide by reflected sunlight, *Appl. Opt.*, *43*, 914–927.

Meredith, M. P., A. C. N. Garabato, A. M. Hogg, and R. Farneti (2012), Sensitivity of the overturning circulation in the southern ocean to decadal changes in wind forcing, *J. Clim.*, *25*, 99–110.

National Research Council (2007), *Earth Science and Applications From Space: National Imperatives for the Next Decade and Beyond*, 456 pp., The National Acad. Press, Washington, D. C. 20001.

Olivier, J., G. Janssens-Maenhout, and J. Peters (2012), *Trends in Global* CO_2 *Emissions*; *2012 Report*, PBL Netherlands Environmental Assessment Agency; Ispra: Joint Research Centre, The Hague, Netherlands.

Olsen, S. C., and J. T. Randerson (2004), Differences between surface and column atmospheric CO_2 and implications for carbon cycle research, *J. Geophys. Res.*, *109*, D02301, doi:10.1029/2003JD003968.

Parazoo, N. C., A. S. Denning, S. R. Kawa, K. D. Corbin, R. S. Lokupitiya, and I. T. Baker (2008), Mechanisms for synoptic variations of atmospheric CO_2 in North America, South America and Europe, *Atmos. Chem. Phys.*, *8*, 7239–7254.

Peters, G. P., G. Marland, C. L. Quéré, T. Boden, J. G. Canadell, and M. R. Raupach (2011), Rapid growth in CO_2 emissions after the 2008–2009 global financial crisis, *Nat. Clim. Change*, *2*, 2–4.

Randerson, J. T., M. V. Thompson, C. M. Malmstrom, C. B. Field, and I. Y. Fung (1996), Substrate limitations for heterotrophs: Implications for models that estimate the seasonal cycle of atmospheric CO_2, *Global Biogeochem. Cycles*, *10*(4), 585–602, doi:10.1029/96GB01981.

Rienecker, M. M., et al. (2011), MERRA: NASA's Modern-Era retrospective analysis for research and applications, *J. Clim.*, *24*, 3624–3648.

Schaaf, C. B., et al. (2002), First operational BRDF, albedo nadir reflectance products from MODIS, *Remote Sens. Environ.*, *83*(1–2), 135–148, doi:10.1016/S0034-4257(02)00091-3.

Schaefer, K., G. J. Collatz, P. Tans, A. S. Denning, I. Baker, J. Berry, L. Prihodko, N. Suits, and A. Philpott (2008), combined simple biosphere/Carnegie-Ames-Stanford approach terrestrial carbon cycle model, *J. Geophys. Res.*, *113*, G03034, doi:10.1029/2007JG000603.

Schaefer, K., T. Zhang, L. Bruhwiler, and A. P. Barrett (2011), Amount and timing of permafrost carbon release in response to climate warming, *Tellus B*, *63*, 165–180, doi:10.1111/j.1600-0889.2011.00527.x.

Shiga, Y. P., A. M. Michalak, S. R. Kawa, and R. J. Engelen (2013), In-situ CO_2 monitoring network evaluation and design: A criterion based on atmospheric CO_2 variability, *J. Geophys. Res. Atmos.*, *118*, 2007–2018, doi:10.1002/jgrd.50168.

Spiers, G. D., R. T. Menzies, J. Jacob, L. E. Christensen, M. W. Phillips, Y. Choi, and E. V. Browell (2011), Atmospheric CO_2 measurements with a 2 μm airborne laser absorption spectrometer employing coherent detection, *Appl. Opt.*, *50*, 2098–2111, doi:10.1364/AO.50.002098.

Takahashi, T., et al. (2002), Global sea-air CO_2 flux based on climatological surface ocean pCO_2, and seasonal biological and temperature effects, *Deep Sea Res., Part II*, *49*(9–10), 1601–1622, doi:10.1016/S0967-0645(02)00003-6.

Tarnocai, C., J. G. Canadell, E. A. G. Schuur, P. Kuhry, G. Mazhitova, and S. Zimov (2009), Soil organic carbon pools in the northern circumpolar permafrost region, *Global Biogeochem. Cycles*, *23*, GB2023, doi:10.1029/2008GB003327.

van der Werf, G. R., J. T. Randerson, L. Giglio, G. J. Collatz, M. Mu, P. S. Kasibhatla, D. C. Morton, R. S. DeFries, Y. Jin, and T. T. van Leeuwen (2010), Global fire emissions and the contribution of deforestation, savanna, forest, agricultural, and peat fires (1997–2009), *Atmos. Chem. Phys.*, *10*, 11,707–11,735, doi:10.5194/acp-10-11707-2010.

Yokota, T., Y. Yoshida, N. Eguchi, Y. Ota, T. Tanaka, H. Watanabe, and S. Maksyutov (2009), Global concentrations of CO_2 and CH_4 retrieved from GOSAT: First preliminary results, *SOLA*, *5*, 160–163, doi:10.2151/sola.2009-041.

Zhang, T., R. G. Barry, K. Knowles, J. A. Heginbottom, and J. Brown (1999), Statistics and characteristics of permafrost and ground-ice distribution in the Northern Hemisphere, *Polar Geogr.*, *23*(2), 132–154.

Zimov, S. A., E. A. G. Schuur, and F. S. Chapin III (2006), Permafrost and the Global Carbon Budget, *Science*, *312*(5780), 1612–1613, doi:10.1126/science.1128908, 16 June.